ORIGINAL PAPER

Some computational aspects for solving deep penetration problems in geomechanics

Daichao Sheng · Majidreza Nazem · John P. Carter

Abstract Penetration problems in geomechanics involve the insertion or intrusion of solid bodies into the ground. Such problems are extremely difficult to model numerically, because they usually involve severe mesh distortion caused by large deformation and frictional contact. In this paper, an Arbitrary Lagrangian–Eulerian method is used to overcome the mesh distortion problem. Some specific issues associated with the ALE method, such as node relocation and remapping of contact history variables, are discussed. The ALE method, incorporated with an automatic load stepping scheme and a smooth contact discretisation technique, is then used to analyse the penetration of axial displacement piles into the ground.

Keywords Penetration problems · Frictional contact · Mesh distortion · ALE method · Mesh motion

1 Introduction

Penetration problems in geomechanics involve the insertion or intrusion of solid bodies into the ground. The solid body can be a displacement pile used to support a structural load or a testing device used to measure soil properties. Numerical modelling of such problems can improve our understanding of the physical processes involved, which in turn can lead to better interpretation of test results and more accurate estimation of pile capacity [9]. However, such a simulation is extremely complex, mainly because the problem involves large deformations that make it difficult to design an appropriate finite element mesh. In principle, the soil elements beneath and around the penetrating body should be sufficiently small to achieve good accuracy in the numerical results. However, the use of fine elements inevitably leads to severe mesh distortion and even negative element Jacobians due to the very large deformation in the soil around the penetrating body.

One of the early attempts to solve penetration problems numerically was made by van den Berg [29], who combined interface elements with an Eulerian formulation of large deformation to model a fixed volume of soil mass streaming past a fixed cone. This method successfully avoided the mesh distortion problem, but it is limited to known material flows at boundaries. Therefore, the method cannot simulate the complete penetration process right from the ground surface. In addition, as with other Eulerian methods where the discretisation does not move with the material, the approach has difficulties in tracking material history. It is thus difficult to model history-dependent material behaviour, such as the stress-path dependence exhibited by many soils. Hu and Randolph [8] presented a novel method that combines small strain analysis with coordinate updating and remeshing. They successfully applied their method to model the penetration of spudcan foundations, and it has the marked benefit of being theoretically straightforward and simple for implementation. However, the efficiency and accuracy of the method for solving problems involving significant rotation need further research. Liyanapathirana et al. [13] presented a new method for modelling the large deformations associated with pile driving. By successively activating predefined soil–pile interface and pile elements, they were able to model the large penetration of open-ended piles with negligible wall thickness. Because the inactive pile and interface elements must be defined a priori, they cannot occupy space when they

D. Sheng (✉) · M. Nazem · J. P. Carter
School of Engineering, The University of Newcastle,
Newcastle, NSW, Australia
e-mail: daichao.sheng@newcastle.edu.au
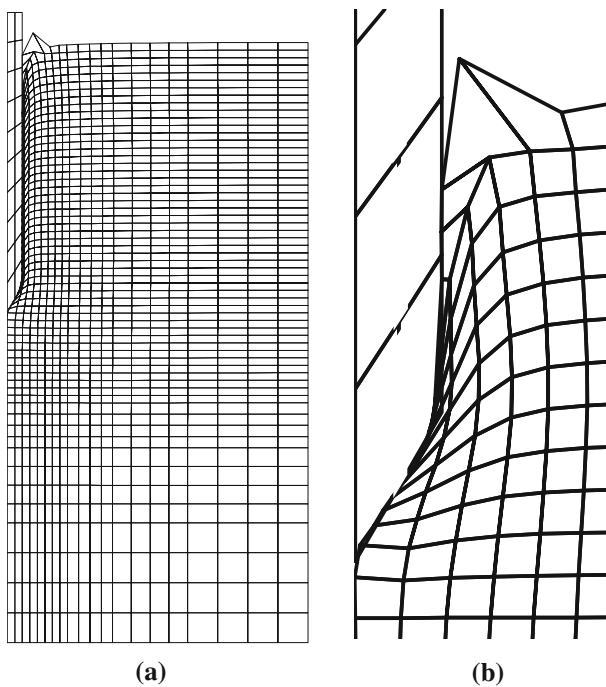
Fig. 1 Mesh for large deformation analysis of pile installation, showing **a** the finest soil elements beneath the pile that are possible for a successful Updated Lagrangian analysis (pile–soil friction coefficient $\mu = 0.1$) and **b** typical mesh distortion if the interfacial frictional coefficient is larger than 0.1

are inactive. It is thus difficult to extend their method to handle closed-ended piles or open-ended piles with a significant wall thickness. In a different approach, Sheng et al. [20,21, 24] used the contact mechanics facility in the commercial code ABAQUS to model cone penetration tests in dry soils, but encountered serious problems with mesh and time step effects. Very coarse elements and extremely small time steps had to be used, leading to inaccurate and time-consuming analyses. For example, it was found that the smallest soil element that can be used in a Lagrangian formulation must have a dimension which is approximately half the radius of the penetrating body. Figure 1a shows a typical deformed mesh from such an analysis assuming axi-symmetric conditions. It can be noted that most radial deformation in the soil occurs within the first annular column of elements around the penetrometer. This deformation pattern indicates the importance of the discretisation of the soil underneath the penetrometer. Although the soil elements should be sufficiently small to capture the localised deformation, further refinement of the soil elements shown in Fig. 1a can cause negative element Jacobians and numerical breakdown. Susila and Hryciw [28] used the remeshing technique in ABAQUS to model static cone penetration tests in a Drucker–Prager material. However, the same problems occurred with mesh fineness and convergence, and the analyses had to assume a rigid penetrometer.

The frictional contact at the soil–structure interface also makes it difficult to obtain a stable, convergent solution. First, the friction at the interface affects the shear deformation in the soil elements around the penetrating body, and higher interfacial friction exaggerates the distortion of these elements. The meshes shown in Fig. 1a are for an interfacial friction coefficient of 0.1. Further increasing this quantity will inevitably lead to unacceptable mesh distortion or negative element Jacobians (Fig. 1b). Second, the sudden change of the normal directions along the penetrating body (at corners or vertices) can cause oscillation of the computed contact forces. For example, it is observed that the computed pile resistances are strongly oscillatory due to the cyclic release of the soil nodes from the pile tip and the shoulder [26,20,24]. A typical example is shown in Fig. 2. The oscillations occur whenever a soil node is released from vertical compression beneath the conical end. Once the soil node moves past the transition point at the shoulder of the pile, the high vertical compression changes largely to a shearing force. Because this shear force is restricted by the friction law at the interface, a sudden drop in the total resistance is expected. Afterwards the resistance increases again until the next soil node moves past the vertex. These sudden changes in the vertical force can lead to divergence of the numerical analysis if they are not handled properly. The magnitude of these sudden changes, of course, depends on the discretisation of the soil beneath and around the pile. In theory, the observed oscillations in the total resistance would vanish if the soil beneath the penetrating cone could be discretised into infinitely small elements.

Another computational challenge in the modelling of penetration problems arises from the large variation of the material stiffness. For example, a soil modelled by the Modified Cam Clay Model has essentially zero stiffness at zero mean stress, such as near the ground surface, but a steel pile has a Young modulus which is of the order of 100 GPa. Very often, the penetrating body is simply treated as a rigid body, to avoid the ill-conditioning of the stiffness matrix. Indeed, it seems that most commercial codes are limited to this approach when they are used to simulate penetration problems [9,21]. This is inconvenient when we are also interested in the stresses in the penetrating body, and thus have to consider its finite stiffness as well.

Very recently, Sheng et al. [24] proposed a number of numerical algorithms to improve the solutions of pile penetration problems. These include a smooth discretisation of the pile surface to enhance the performance of node-to-segment contact elements, and an automatic load stepping scheme for linearisation of the discretised governing equations. Although these algorithms have led to significant improvement of the numerical solutions in terms of robustness and efficiency, the fundamental problem of mesh distortion remains to be solved.

Fig. 2 Oscillation in predicted pile resistance and the sudden change of contact stresses at the vertex (pile radius = 0.2 m)
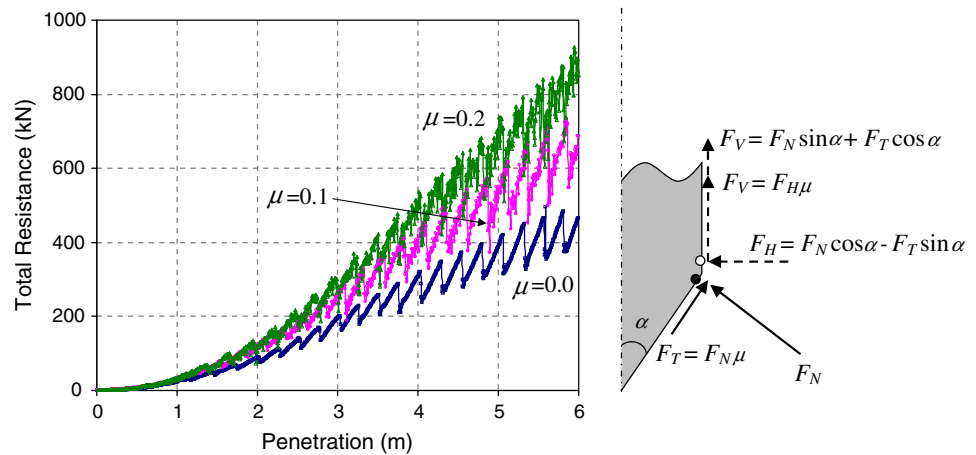
An effective method to tackle the mesh distortion in large deformation problems is the so-called Arbitrary Lagrangian–Eulerian method. The ALE method is based on the separation between material and mesh displacements [2,3,6,7,12,32]. Such an ALE method typically involves two substeps during every time step: a Lagrangian step followed by an Eulerian step. In the Lagrangian step, the governing equations are solved to obtain the material displacements. At the end of this step, the mesh may be distorted. In the Euler step, a new and better mesh is generated for the deformed domain to obtain the mesh displacements. All kinematic and static variables are then transferred from the distorted mesh to the new mesh. The key issues in this method thus include the mesh refinement method and the remapping of variables between the two meshes.

The method used in this paper closely follows that recently proposed by Nazem et al. [16] and Sheng [25], but includes some improvements to their node relocation scheme. The key challenge when applying this ALE method to frictional contact problems is the remapping of history variables for all the contact elements. Such variables include the elastic and plastic slip functions of each slave node. The ALE method is then incorporated into an automatic load stepping scheme with the smooth contact discretisation technique presented by Sheng et al. [24] and Sheng [25]. The effectiveness of these numerical enhancements is demonstrated by simulations of the installation of displacement piles.

2 Arbitrary Lagrangian–Eulerian method

2.1 Updated Lagrangian solution

The Arbitrary Lagrangian–Eulerian (ALE) method used here is based on the operator-split technique [2,16] and is associated with the Updated Lagrangian (UL) formulation. We thus first briefly review the UL formulation of large deformations.

For simplicity, we limit our discussion to time-independent problems of a single phase soil that does not involve pore pressure dissipation.

In order to accommodate the definitions of stress rates, we use index notation in this part of the paper. The index notation is then changed to vector and matrix notation in the following section, to facilitate the expressions for time stepping and iterations when solving the global equations.

The principle of virtual work states that if δu is a virtual displacement field satisfying the displacement boundary conditions, then equilibrium is satisfied provided:

$$\sum_\alpha \left(-\int_{V_\alpha} \sigma_{ij}\delta\varepsilon_{ij}\mathrm{d}V + \int_{V_\alpha} \delta u_i b_i \mathrm{d}V + \int_{S_\alpha} \delta u_i q_i \mathrm{d}S \right)$$
$$+ \int_{S_c} (t_N \delta g_N + t_T \delta g_T)\mathrm{d}S = 0 \tag{1}$$

where $\delta\varepsilon$ denotes the variation of the strain tensor derived from the virtual displacements, σ is the Cauchy stress tensor, b the body force vector, q the distributed force acting on the boundary S_α of the volume V_α, t_N and t_T are respectively the normal and tangential forces at the contact surface S_c, δg_N and δg_T are respectively the virtual normal and tangential gap, and the summation is over the number of bodies. For a nonlinear problem, Eq. 2 is typically applied incrementally. We assume that the analysis starts at time 0 and all state variables that satisfy equilibrium are known up to time t. Further loading and deformation will require the equilibrium to be satisfied at time $t + \Delta t$. The principle of virtual work becomes:

$$\sum_\alpha \int_{V_\alpha^{t+\Delta t}} \sigma_{ij}^{t+\Delta t}\delta\varepsilon_{ij} \cdot \mathrm{d}V = R^{t+\Delta t} + C^{t+\Delta t} \tag{2}$$

where R denotes the virtual work resulting from body forces and surface tractions, C denotes the virtual work resulting from the contact tractions, and the superscript denotes the time when the quantities are measured. The quantity R

involves a volume integration over $V^{t+\Delta t}$ and a surface integration over $S^{t+\Delta t}$. The quantity C involves surface integrations over the contact surface ($S_c^{t+\Delta t}$). For geometrically nonlinear problems, the configuration ($V^{t+\Delta t}$ and $S^{t+\Delta t}$) in Eq. 2 is not known and has to be transferred to a known configuration, for example the one at the start of the current time step t (Updated Lagrangian) or the one at time zero (Total Lagrangian). In either case, the second Piola–Kirchhoff stress and the Green–Lagrangian strain are usually introduced in place of σ and ε, respectively, to eliminate the effects of rigid body motion on the Cauchy stress tensor.

For problems involving large-slip contact, the contact constraints are always described using the current configuration and therefore the Updated Lagrangian formulation is preferable. Since constitutive laws for geomaterials can seldom be written conveniently in terms of the second Piola–Kirchhoff stress and the Green–Lagrangian strain, we decompose the Cauchy stress rate into a frame-independent stress rate due to straining and a stress rate due to rigid body motion. Using the Jaumann stress rate as the frame-independent stress rate, we have

$$d\sigma_{ij}^J = d\sigma_{ij} - \sigma_{ik}d\Omega_{kj} - \sigma_{jk}d\Omega_{ki} = C_{ijkl} \cdot d\varepsilon_{kl} \quad (3)$$

where C_{ijkl} is the stress–strain tensor derived from the constitutive relations in terms of the Cauchy stresses and the linear strains, and Ω is the spin tensor given by

$$\Omega_{ij} = \frac{1}{2}\left(\frac{\partial u_i}{\partial x_j} - \frac{\partial u_j}{\partial x_i}\right) \quad (4)$$

Introducing (3) into the virtual work equation, we obtain the following equilibrium equation for the UL method based on the Jaumann stress rate according to

$$\int_{V^t} C_{ijkl}d\varepsilon_{kl}\delta\left(d\varepsilon_{ij}\right)dV^t$$
$$+ \int_{V^t}\left(\sigma_{ik}^t d\Omega_{kj} + \sigma_{jk}^t d\Omega_{ki}\right)\delta\left(d\varepsilon_{ij}\right)dV^t$$
$$+ \int_{V^t}\sigma_{ij}^t\delta\left(d\eta_{ij}\right)dV^t$$
$$= R^{t+\Delta t} + C^{t+\Delta t} - \int_{V^t}\sigma_{ij}^t\delta\left(d\varepsilon_{ij}\right)dV^t \quad (5)$$

where $\delta(d\eta)$ is the variation of the nonlinear part of the incremental Green–Lagrange strain tensor. Linearisation of the terms on the left-hand side in the above equation will generally lead to a stiffness matrix corresponding to material non-linearity (the first integration on the left-hand-side) as well as a stiffness matrix corresponding to the geometric nonlinearity (the second and third integrations on the left-hand-side). Linearisation of the virtual work due to contact

tractions requires the discretisation of the contact surfaces, which will be discussed later.

At Gauss points, the stress increments are found by integrating $d\sigma_{ij}$ in Eq. 3 along given strain increments and spin tensor increments. Nazem et al. [16] have recently discussed alternative integration schemes for geomaterials that experience strain hardening.

2.2 ALE solution

At the end of the Updated-Lagrangian solution outlined above, the mesh may be distorted since it moves along with the material. To avoid mesh distortion, the mesh and the material displacements can be separated from each other, thus allowing the mesh to move independently from the material. This assumption leads to the formulation of the Arbitrary Lagrangian–Eulerian (ALE) method, which adds an additional Euler step following each UL step. In the Euler step, a new mesh is generated for the deformed domain. All kinematic and static variables are then transferred from the old mesh to the new mesh using the relation between the material derivative and the mesh derivative [16]

$$\dot{f} = \dot{f}^r + \left(v_i - v_i^r\right)\frac{\partial f}{\partial x_i} \quad (6)$$

where f is an arbitrary function, v_i is the material velocity, v_i^r the mesh velocity, $\dot{f}$ denotes the time derivative of f with respect to material coordinates, and $\dot{f}^r$ represents the time derivative of f with respect to mesh (grid points) coordinates. The term $v_i - v_i^r$ is called the convective velocity.

Because the mesh displacements are decoupled from the material displacements, we can see that the new mesh to be established in the Euler step can be arbitrary, provided two basic conditions are satisfied:

1. The new mesh should conform to the deformed boundaries of the domain and the materials.
2. The topology and connectivity of the new mesh should remain the same as the old mesh.

These requirements ensure that the mapping of variables between the new and old meshes can be carried out material-by-material and element-by-element. The first requirement also implies that the nodes on a material or domain boundary should remain on it, even though the locations of other internal nodes in the new mesh are arbitrary. We also notice that, for an initially optimal mesh for a homogeneous domain, if the displacements at all the boundary nodes are prescribed and such displacements ensure an optimal division of the boundaries, then an elastic analysis based on the prescribed displacements should result in an optimal distribution of internal nodes. Here the word 'optimal' loosely means that the mesh quality is as good as the undeformed
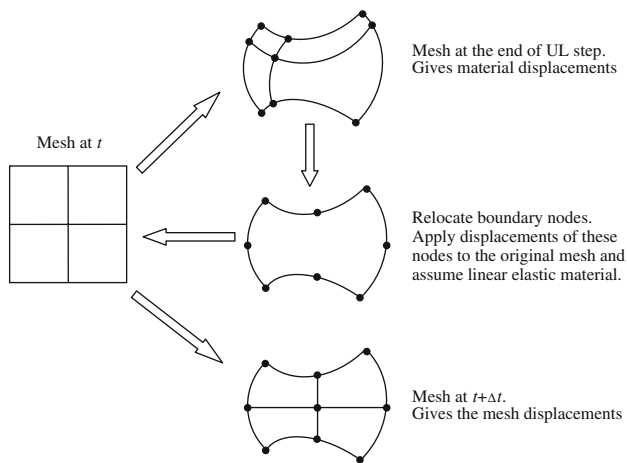
Fig. 3 General procedure of the ALE node relocation method

mesh. Because the displacements at all boundary nodes are prescribed, the elastic properties used in such an analysis may be arbitrary as long as the material is assumed to be homogeneous and isotropic. With these results in mind, our first goal in the Euler step is then to obtain the optimal division of the material and domain boundaries obtained from the UL step, or in other words, to relocate the nodes on the boundaries so that they are optimally located. We also assume that the initial mesh before the UL step is optimal. Comparing the relocated nodes with the nodes in the initial mesh gives us the mesh displacements of the nodes on all the boundaries. With the boundary displacements now known, we carry out an elastic analysis on the initial mesh to obtain the optimal mesh displacements of the internal nodes. Because we prescribe the displacements along all boundaries and material interfaces, the actual values of the elastic parameters used in this analysis are not important, as previously indicated, and one set of elastic parameters can be used for the entire domain, regardless of the presence of real material interfaces. The new mesh so obtained also shares the same connectivity and topology as the old mesh. The procedure outlined above is illustrated in Fig. 3.

Once the mesh displacements are obtained, the state variables such as stresses and hardening parameters are then transferred to the new mesh. The general procedure for the ALE method consists of the following steps.

1. Perform an UL step to find the material displacements.
2. Relocate the nodes on all boundaries of the domain and between materials.
3. Optimise the mesh by performing an elastic analysis.
4. Remap history variables from the old mesh onto the new mesh.

The total nodal displacements are then the summation of the material and mesh displacements. The history variables

remapped to the new mesh can be state variables, such as stresses and hardening parameters, or nodal variables such as displacements. If the stresses and hardening parameters are remapped, the consistency condition may not be satisfied and the objectivity of the solution is not guaranteed. If the displacements are remapped, the stresses and hardening parameters have to be re-integrated over the accumulated strains and hence it is very difficult to deal with initial stresses and stress-path dependence [17,18]. Neither method will guarantee the equilibrium at the end of Step 4. In addition, when frictional contact is involved, history variables such as elastic and plastic slip have to be remapped to the new mesh, giving another potential source of equilibrium imbalance. If equilibrium is indeed not satisfied, additional iterations may be carried out at the end of Step 4 to reduce the unbalanced forces. These iterations can be done with the fixed mesh, i.e., under the assumption of small deformation. The resulting displacements from these iterations are then added to the total nodal displacements. Further details on node relocation and the mapping of history variables may refer to [16].

2.3 Remapping of contact history variables

The procedure for remapping state variables, such as stresses and hardening parameters, follows that suggested in Nazem et al. [16] and Nazem [15]. Since the stiffness of a penetrating structure is usually much larger than that of the soil involved, we can reasonably assume that the distortion of the structure elements is negligible. When the surface of the structure is taken as the master surface and the soil nodes on it are taken as slave nodes [24], the master segments remain unchanged when the slave is relocated during the mesh motion step of the ALE method. This feature significantly simplifies the remapping of contact history variables, and the only one that has to be remapped is the slip function at each slave node. This slip function records the total tangential distance that the slave node has slid along the master surface.

Consider a slave (soil) surface coming into contact with a master (structure) surface, as shown in Fig. 4. The slave surface consists of the slave nodes S1–S5, while the master surface is defined by the nodes M1–M4. The current locations of slave nodes S1–S5 represent the UL solution and
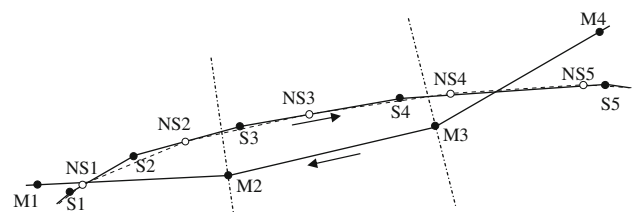
Fig. 4 Relocation of slave nodes (*arrows* indicate the relative movement of master and slave surfaces)

the new slave nodes NS1–NS5 represent their new locations after the node relocation algorithm. With the slip functions at nodes S1–S5 known, the slip functions at nodes NS1–NS5 can be found by interpolation. Before the interpolation is done, a contact search has to be performed to identify the new slave nodes that come into contact with a master segment. In Fig. 4, the slip function at NS2 can be interpolated from the slip functions of S2 and S3. If NS1 comes into contact with the segment M1–M2, its slip function is then set to zero. On the other hand, the slip function at NS4 is preferably extrapolated from those at S3 and S4, instead of interpolating between S4 and S5. In either case, remapping the slip functions at slave nodes is likely to cause some drift from equilibrium, just as the remapping of other state variables may do so. Therefore, an additional equilibrium check after remapping of all state and history variables is recommended.

3 Discretisation of contact surfaces and governing equations

Linearisation of the virtual work equation (1) or (5) requires the linearisation of the virtual work due to contact forces, which in turn requires the discretisation of the contact surfaces [31,11]. In this paper, the so-called node-to-segment contact element is used, where contact constraint is enforced for each slave node while the master surface is discretised into curved segments. The smooth discretisation of the master surface uses BÉZIER polynomials [24]. The discretised virtual work due to normal and tangential contact forces respectively takes the form

$$C_N = \int_{S_c} t_N \delta g_N \, dS \approx \sum_{s=1}^{n_c} \delta \mathbf{u}_s^T [\varepsilon_N A_s g_{N_s} \mathbf{B}_N(\xi)]$$

$$= \sum_{s=1}^{n_c} \delta \mathbf{u}_s^T \mathbf{F}_{Ns}^c \tag{7}$$

$$C_T = \int_{S_c} t_T \cdot \delta g_T dS \approx \sum_{s=1}^{n_c} \delta \mathbf{u}_s^T \mathbf{B}_\xi(\xi) \left\| \frac{\partial \bar{\mathbf{x}}_s}{\partial \xi} \right\| \gamma A_s$$

$$= \sum_{s=1}^{n_c} \delta \mathbf{u}_s^T \mathbf{F}_{Ts}^c \tag{8}$$

where n_c is the total number of slave nodes, $\delta \mathbf{u}_s$ the nodal virtual displacements of the contact element consisting of one slave node and two master nodes, A_s the contact area associated with the slave node, ε_N the penalty parameter for normal contact, g_{N_s} the normal gap, γ the tangential stress which will depend on the constitutive law for slip contact and on the tangential penalty parameter for stick contact, $\bar{\mathbf{x}}_s$ are the coordinates of the projection of the slave node on the master segment, ξ the distance between $\bar{\mathbf{x}}_s$ and the master

node that is closest to the slave node, $\mathbf{B}_N$ and $\mathbf{B}_\xi$ are BÉZIER polynomials, and $\mathbf{F}_{Ns}^c$ and $\mathbf{F}_{Ts}^c$ are the nodal forces of the contact element.

The linearisation of equations (7) and (8) gives the element tangent matrices for normal and tangential contact. Combining equations (1), (7) and (8) leads to a set of global equations of the form

$$\sum_\alpha \left(-\int_{V^\alpha} \delta \boldsymbol{\varepsilon}^T \boldsymbol{\sigma} \, dV + \int_{V^\alpha} \delta \mathbf{u}^T \mathbf{b} \, dV \right.$$

$$\left. + \int_{S_\sigma^\alpha} \delta \mathbf{u}^T \mathbf{t} \, dS \right) + \int_{S_c} (t_N \delta g_N + t_T \delta g_T) \, dS$$

$$= \delta \mathbf{U}^T \left(\mathbf{G}(\mathbf{U}) + \mathbf{F}_N^c(\mathbf{U}) + \mathbf{F}_T^c(\mathbf{U}) \right)$$

$$= \delta \mathbf{U}^T \left(\mathbf{G}(\mathbf{U}) + \mathbf{G}^c(\mathbf{U}) \right) = \delta \mathbf{U}^T \mathbf{R}(\mathbf{U}) = \mathbf{0} \tag{9}$$

where $\mathbf{U}$ is used in place of $\mathbf{u}$ to indicate the discretised global displacement field, $\mathbf{G}(\mathbf{U})$ denotes the domain contributions to the residual vector, $\mathbf{G}^c(\mathbf{U})$ denotes the contact contributions given by (7) and (8), and $\mathbf{R}(\mathbf{U})$ is the global residual vector.

The global tangent matrix is obtained by linearising (9) at a given $\mathbf{U}$ according to

$$\mathbf{K}(\mathbf{U}) = \frac{\partial \mathbf{R}(\mathbf{U})}{\partial \mathbf{U}} = \frac{\partial \left(\mathbf{G}(\mathbf{U}) + \mathbf{G}^c(\mathbf{U}) \right)}{\partial \mathbf{U}}$$

$$= \left(\mathbf{K}_{ep}(\mathbf{U}) + \mathbf{K}_{nl}(\mathbf{U}) + \mathbf{K}_{Ns}(\mathbf{U}) + \mathbf{K}_{Ts}(\mathbf{U}) \right) \tag{10}$$

where $\mathbf{K}_{ep}$ is the stiffness matrix due to the material stiffness, $\mathbf{K}_{nl}$ the stiffness matrix due to geometric nonlinearity, and $\mathbf{K}_{Ns}$ and $\mathbf{K}_{Ts}$ are the tangent matrices due to normal and tangential contact.

With the material, geometry and contact stiffness matrices derived, the automatic load stepping scheme presented in [24] can then be modified to solve equation (9). The modified algorithm is presented below. Note that the Euler step in the ALE method includes the steps 4.7–4.12 in the algorithm below. If the sub-increment is large enough to cause significant mesh distortion, these steps can also be included in each sub-increment within each coarse increment. In addition, an equilibrium check can be included at the end of step 4.11. If equilibrium is not satisfied, additional iterations may be carried out before Step 12, to reduce the unbalanced forces.

In the algorithm below, steps 4.1–4.8 represent the Lagrangian step, and steps 4.9–4.13 represent the Eulerian step in the ALE method. The automatic stepping scheme is carried out in step 4.5, where two user-defined tolerances are used to control the step size error: *DTOL* and *ITOL*.

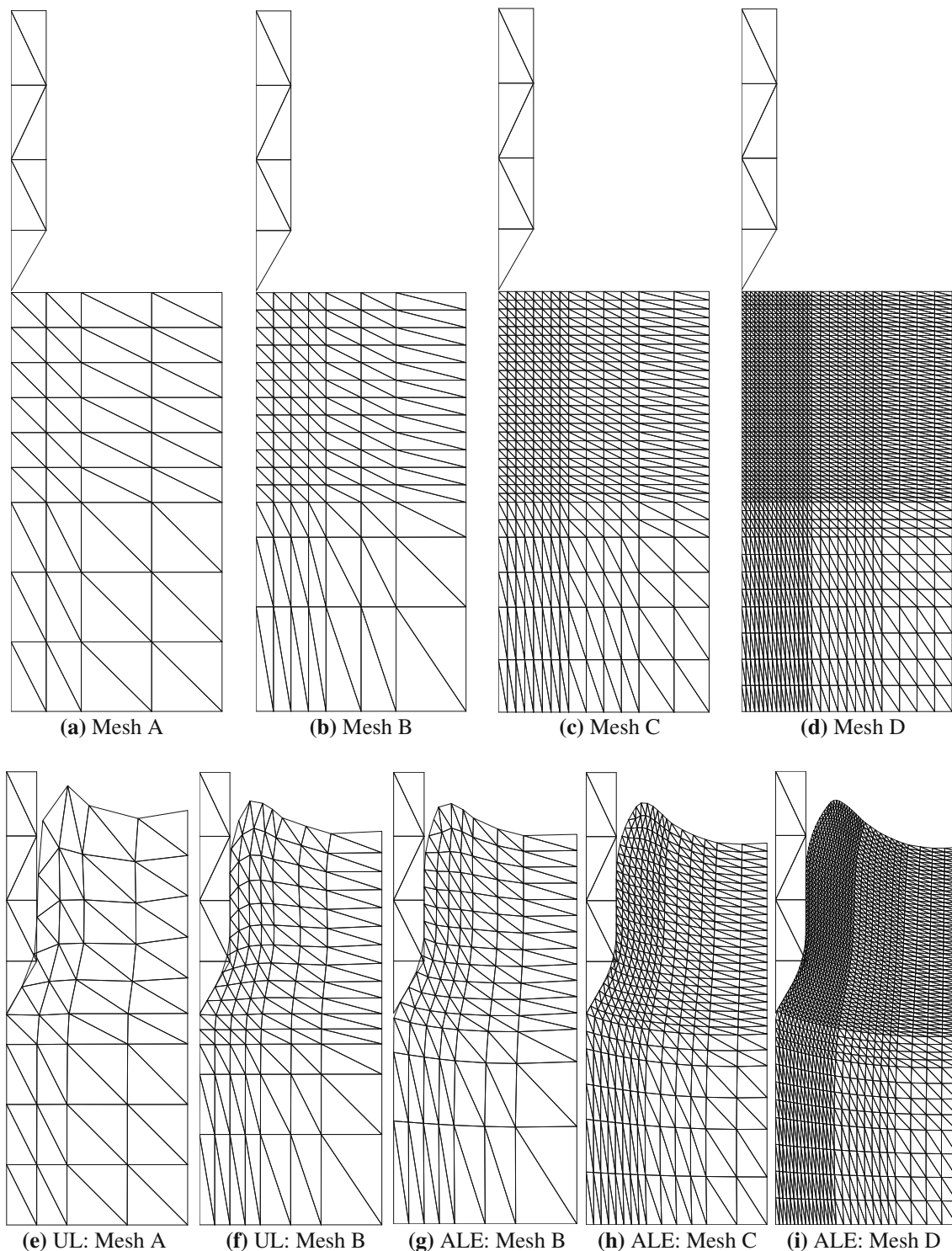**Algorithm—automatic load stepping incorporated into the ALE method**

1. Initialise algorithm: set $\mathbf{U=0.}$

2. Check for contact: $g_{Ns}^{0} \leq 0 \;\; \rightarrow \;\;$ active node .

3. Set all active nodes to state of 'stick'.

4. LOOP over coarse load steps: $n = 1, \ldots$

    4.1. Solve: $\Delta\mathbf{U}_{1} = \left[\mathbf{K}(\mathbf{U}_{n-1})\right]^{-1}\left(\mathbf{F}_{n}^{ext} - \mathbf{F}_{n-1}^{ext}\right)$ and update $\mathbf{U}_{n} = \mathbf{U}_{n-1} + \Delta\mathbf{U}_{1}$.

    4.2. Check for contact: $g_{Ns}^{n} \leq 0 \;\; \rightarrow \;\;$ active node .

    4.3. Solve: $\Delta\mathbf{U}_{2} = \left[\mathbf{K}(\mathbf{U}_{n-1} + \Delta\mathbf{U}_{1})\right]^{-1}\left(\mathbf{F}_{n}^{ext} - \mathbf{F}_{n-1}^{ext}\right)$.

    4.4. $R = \dfrac{1}{2}\dfrac{\|\Delta\mathbf{U}_{2} - \Delta\mathbf{U}_{1}\|}{\|\mathbf{U}_{n}\|}$

    4.5. IF $R \leq DTOL$, iteration $i = 1, \ldots,$ convergence.

        4.5.1. Check for convergence $\|\mathbf{R}(\mathbf{U})\| \leq ITOL \cdot \|\mathbf{F}^{ext}\| \;\Rightarrow\;$ exit iteration with a new step size for next substep.

        4.5.2. Solve: $\delta\mathbf{U}^{i} = \left(\mathbf{K}(\mathbf{U}_{n}^{i-1})\right)^{-1}\mathbf{R}(\mathbf{U}_{n}^{i-1})$.

        4.5.3. Update $\Delta\mathbf{U}_{1}^{i} = \Delta\mathbf{U}_{1}^{i-1} + \delta\mathbf{U}^{i}$ and $\mathbf{U}_{n}^{i} = \mathbf{U}_{n-1} + \Delta\mathbf{U}_{1}^{i}$.

        4.5.4. Check for contact: $g_{Ns}^{n} \leq 0 \;\; \rightarrow \;\;$ active node .

    4.6. ELSE, reduce step size and restart step 4.1.

    4.7. ENDIF.

    4.8. Update material coordinates $\mathbf{X}_{M} = \mathbf{X}_{M} + \mathbf{U}$.

    4.9. Compute nodal stresses using a stress recovery procedure.

    4.10. Check the boundaries and relocate the nodes on them wherever necessary.

    4.11. Compute the new mesh coordinates by performing an elastic analysis and store them in $\mathbf{X}_{G}$.

    4.12. Remap state variables and contact history variables onto the new mesh.

    4.13. Update the total displacements vector by $\mathbf{U} \leftarrow \mathbf{U} - \mathbf{X}_{M} + \mathbf{X}_{G}$.

5. END LOOP.

4 Numerical examples

The first example is a purely academic problem where the effects of the mesh fineness and the ALE method on the solution are studied. A relatively short pile is chosen to reduce the computational work. The finite element meshes and material properties adopted in the analyses are shown in Fig. 5. Linear triangular elements are used both for the soil and the pile. Higher order elements could be used here, but in such cases special techniques have to be used to ensure the contact forces are transferred correctly [31]. Four types of mesh are used,

with the ratio between the width of the soil elements beneath the pile and the pile radius varying between 0.125 to 1.

An elastic pile of radius 0.4 m is pushed into the soil to a depth of 2.0 m. The penetration is achieved by imposing a total vertical displacement at the two top nodes of the pile shaft. The soil is modelled as a non-associated Mohr–Coulomb material, with the properties given in Fig. 5. The pile is modelled as an elastic material with a Young's modulus $E = 2 \times 10^{8}$ kPa, which is 2×10^{4} times the modulus of the soil. Other material properties defined in Fig. 5 are: $\nu = $ Poisson's ratio, $c' = $ cohesion, $\phi' = $ frictional angle, $\psi' = $

(a) Mesh A   **(b)** Mesh B   **(c)** Mesh C   **(d)** Mesh D

(e) UL: Mesh A   **(f)** UL: Mesh B   **(g)** ALE: Mesh B   **(h)** ALE: Mesh C   **(i)** ALE: Mesh D

Fig. 5 Original and deformed meshes (Mohr–Coulomb soil: $E = 10^4$ kPa, $\nu = 0.3$, $c' = 1$ kPa, $\phi' = 30^o$, $\psi' = 20^o$, $\gamma = 20$ kN/m^3. Elastic pile: $E = 1.0 \times 10^8$ kPa, $\nu = 0.3$. Dimension of initial soil domain: 2.4 m × 4.8 m. Dimension of pile shaft: 0.4 m × 3 m. Cone angle: 60°. Pile–soil interfacial friction coefficient: 0.01. Penetration: 2.5 m)

dilation angle, and $\gamma =$ unit weight of the soil. The pile-soil interfacial friction coefficient is set to 0.01. The penalty parameters in the normal and tangential directions are set to 10^6 kN/m^3. It was found that this value can be increased or decreased by an order of one, without causing significant change in the numerical results.
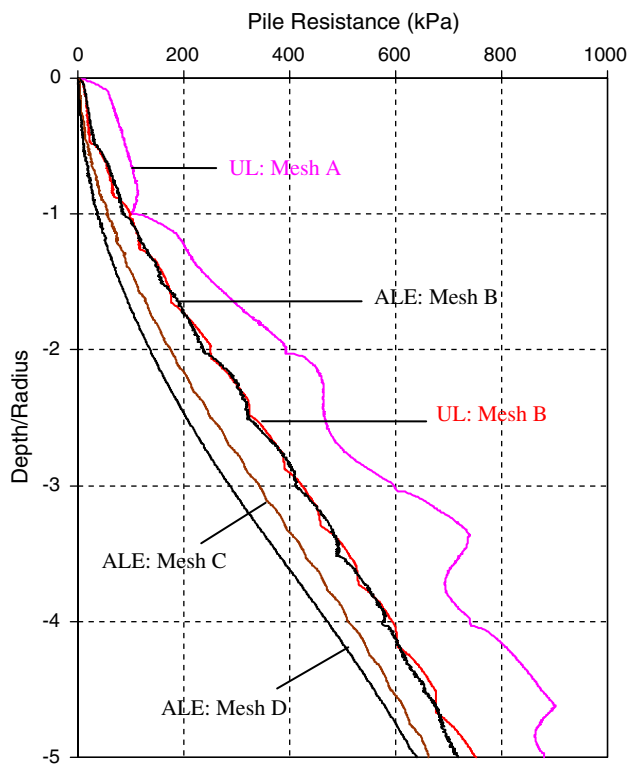
Fig. 6 Mesh effects on the pile resistances

The Updated Lagrangian method was employed to analyse mesh A and mesh B shown in Fig. 5a and b, respectively. The deformed meshes from the UL analyses are illustrated in Fig. 5e and f, respectively. In addition, the Arbitrary Lagrangian–Eulerian method was also used to analyse the same meshes. Figure 5g shows the deformed mesh from the ALE analysis for mesh B. This is not much different from the mesh in Fig. 5f, except that the nodes along the boundaries as well as the internal nodes are relocated. The meshes shown in Fig. 5h and i were also obtained from ALE analyses.

Figure 6 shows the predicted pile resistances as a function of the depth of penetration for the four meshes. As expected, the UL and ALE analyses give almost the same curve for Mesh B. At any penetration depth the predicted pile resistance decreases as the mesh becomes finer. The predicted resistances for mesh A differ from those for mesh D by up to a factor of 2. However, the differences between Mesh C and Mesh D are not as pronounced as those between mesh A and mesh B, indicating that the numerical solution is converging as the mesh is refined. The difference (∼15%) between the results for mesh C and D indicates that very fine elements have to be used in such analyses. It is believed that the convergence rate will improve as the soil becomes less dilatant (e.g., a soil modelled by the modified Cam clay model). It is also observed that the numerical oscillations in the predicted pile resistances become less pronounced for the finer meshes such as C and D.

In the second example, a steel pile of radius 0.2 m is pushed into a Mohr–Coulomb soil to a depth of 2.5 m. The finite element mesh shown in Fig. 7, where the width of the finest soil elements is roughly one eighth of the pile radius, was used for the ALE analysis. Figure 7 indicates that the ALE analysis can simulate the penetration of the pile to a depth of 12.5 pile radii without generating any significant or unwanted mesh distortion. Four-noded linear elements are used in the analysis. Due to the dilatant behaviour predicted by the Mohr–Coulomb model under shear, the total volume of the soil increases as the pile is inserted. The volume increase can be confirmed by estimating the total volume occupied by all soil elements in Fig. 7.

In Fig. 8, the predicted total resistances, i.e. the reactions at the two top nodes where displacements are prescribed, are plotted against the normalised penetration depth. All UL solutions in the figure are obtained using a coarser mesh with the width of the finest soil elements equal to one quarter of the pile radius. With such a coarse mesh, the UL analysis can also furnish with some results, provided that steps with unbalanced forces larger than the prescribed tolerance are allowed to continue. The predicted total resistance from the UL analysis shows strong oscillations, similar to those shown in Fig. 2. The UL analysis using unsmoothed pile segments cannot finish with a complete solution, due to severe mesh distortion. Comparing the curves denoted by UL ($\mu = 0.1$, unsmoothed pile segments) and UL ($\mu = 0.1$), we see that the smooth discretisation of the contact surfaces reduces the oscillations significantly. Comparing the curves denoted by UL ($\mu = 0.1$) and UL ($\mu = 0.0$), we see that the degree of oscillation depends also on the amount of pile–soil interfacial friction.

The ALE solutions illustrated in Fig. 8 were obtained using the smooth discretisation of the contact surfaces. These solutions, even though still somewhat oscillatory, are much smoother than the UL solutions. In theory, to completely remove the oscillations, we need to use very fine soil elements. A key advantage of the proposed ALE method is that it can effectively solve the oscillation problem by using a fine mesh.

In Fig. 9 the computed total resistance is compared with the analytical solution for cone penetration test by Yu [33]. The soil is now represented by the Tresca model with the undrained shear strength of 100 kPa. The soil–cone interface is assumed to be frictionless. The analytical solution of Yu [33] is based on cylindrical cavity expansion theory and is for steady state cone penetration only, i.e., it does not consider the penetration near the ground surface. Figure 9 shows that the computed cone resistance is somewhat larger than the analytical solution for a smooth cone. This overestimation is likely due to the linear elements used for in the analysis. This type of elements is known to be 'locking' in axisymmetric problems and higher order elements should be used to avoid
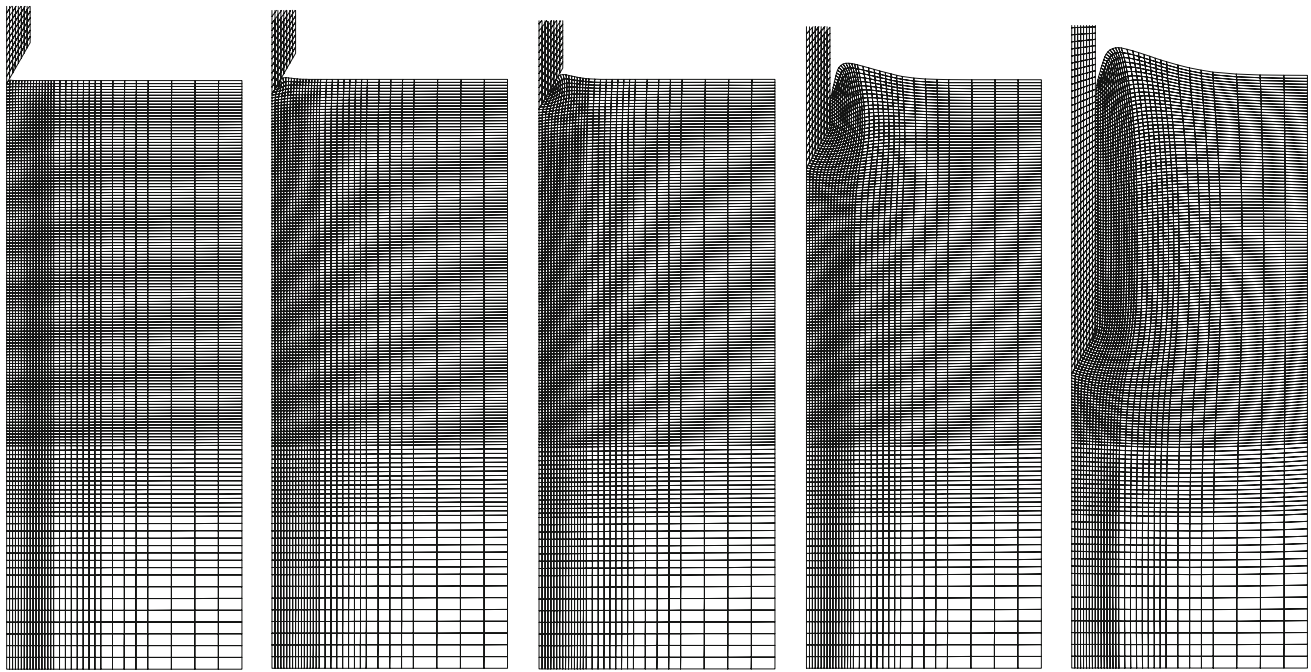
Fig. 7 Deformed meshes (Mohr–Coulomb soil: $E = 10^4$ kPa, $\nu = 0.3$, $c' = 10$ kPa, $\phi' = 35°$, $\psi' = 10°$, $\gamma = 20$ kN/m³. Elastic pile: $E = 1.0 \times 10^8$ kPa, $\nu = 0.3$. Dimension of initial soil domain: 2 m × 5 m. Dimension of pile shaft: 0.2 m × 3 m. Cone angle: 60°. Pile–soil friction coefficient: 0.1. Penetration: 2.5 m)
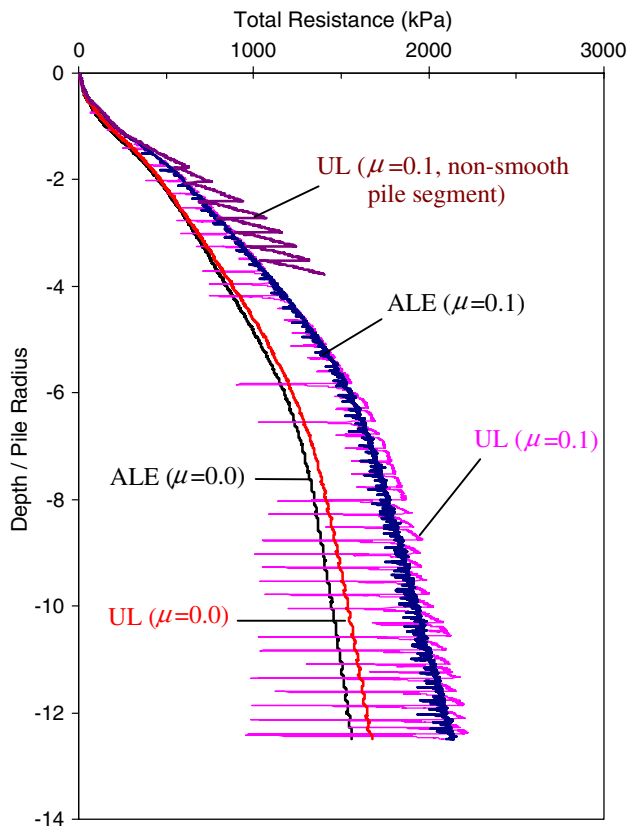
Fig. 8 Predicted load–displacement curves (μ: interfacial friction coefficient. The UL solutions were obtained with a coarser mesh)
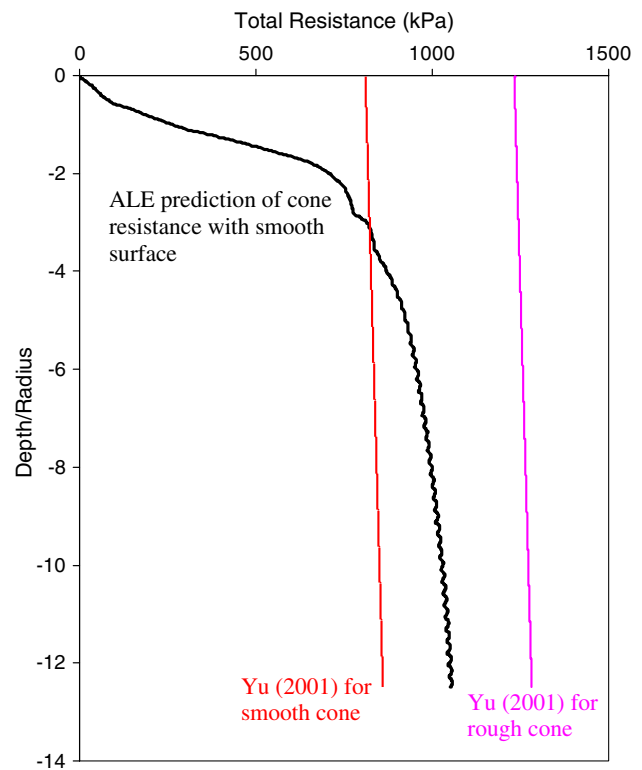
Fig. 9 Predicted load–displacement curve (Tresca soil: $E = 10^4$ kPa, $\nu = 0.4$, $c = 100$ kPa, $\gamma = 20$ kN/m³. Elastic pile: $E = 2.0 \times 10^8$ kPa, $\nu = 0.3$. Dimension of pile shaft: 0.2 m × 3 m. Cone angle: 60°. Pile–soil friction coefficient: 0)
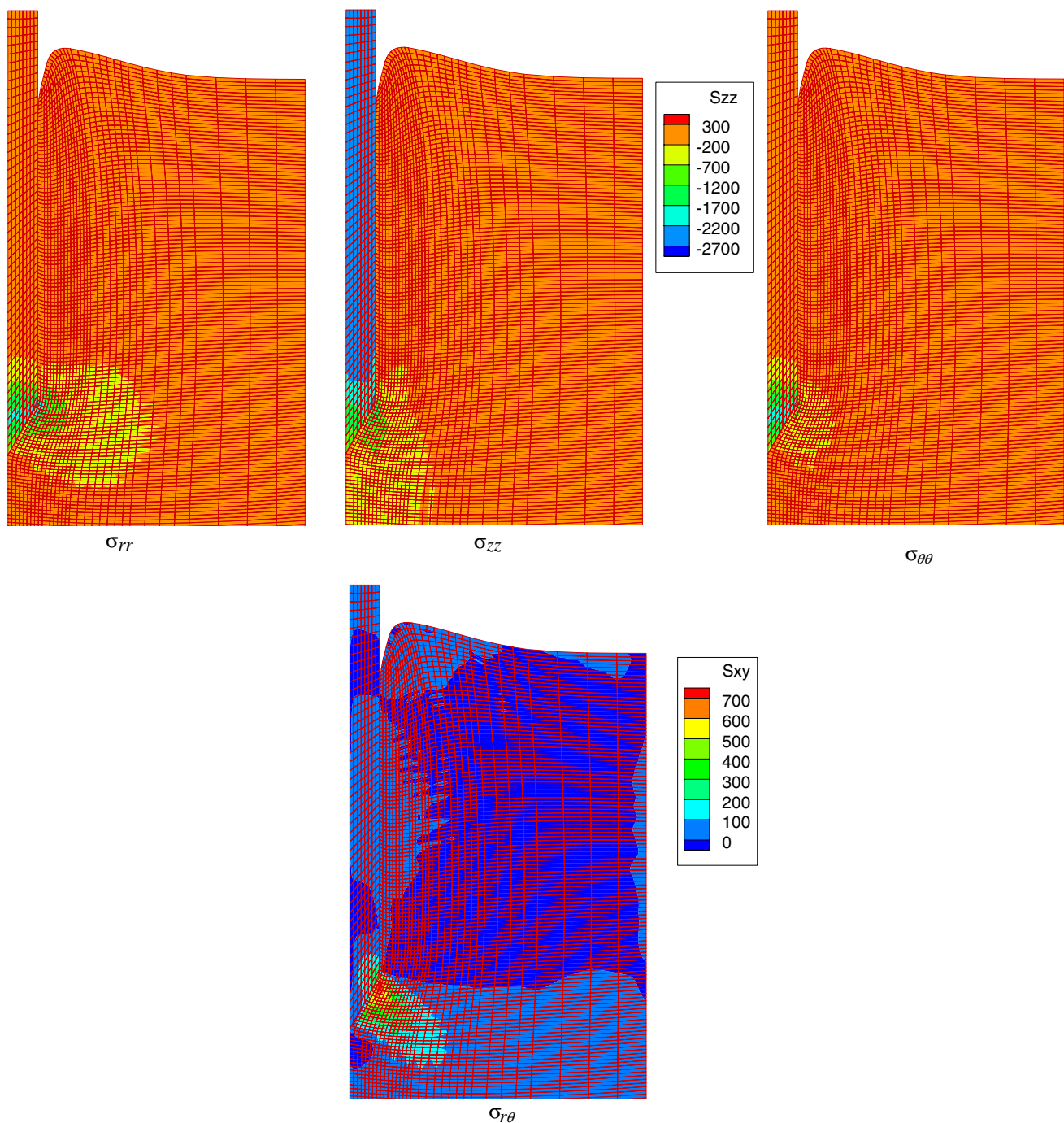
Fig. 10 Stress distributions obtained from ALE analysis (σ_{rr}: radial stress; σ_{zz}: axial stress; $\sigma_{\theta\theta}$: circumferential stress; $\sigma_{r\theta}$: shear stress; legends in kPa and tension positive; Soil: Mohr–Coulomb; Pile: elastic; Pile–soil friction coefficient: 0.1)

the locking [27]However, higher order elements require more complex contact formulation [4,5].

Figure 10 shows some stress contours in the soil and the pile. The stress bulbs beneath the pile are clearly shown in the figures for radial, vertical and circumferential stresses. The shear stress also shows a concentration area beneath the pile end. In the pile, the maximum radial and circumferential stresses occur in the pile end, while the largest vertical stress occurs at the pile shoulder. The key advantage here is that the pile is treated as a deformable body, compared to the rigid piles assumption in the analyses of [26] or [20], Sheng 2004). Some element overlapping is observed near the tip. The overlapping is caused by the penalty method and the smooth discretisation of the pile surface.
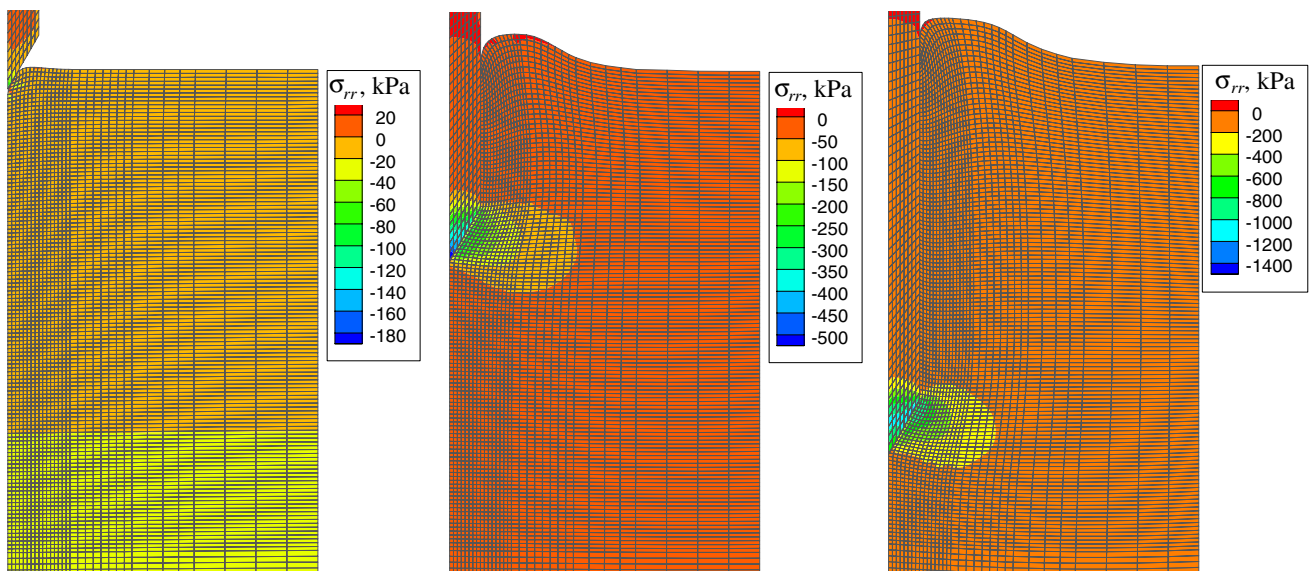
Fig. 11 Radial stress distributions around a pile pushed into Modified Cam Clay (Elastic pile: $E = 10^8$ kPa, $\nu = 0.3$, shaft radius = 0.2 m, length = 3.5 m. Mohr–Coulomb soil: 0.05 m thick, $E = 10^4$ kPa, $\nu = 0.3$, $c' = 1$ kPa, $\phi' = 30^o$, $\psi' = 20^o$, $\gamma = 20$ kN/m^3. Modified Cam Clay soil: 4.95 m thick, $\nu = 0.3$, $\phi' = 30^o$, $\gamma = 20$ kN/m^3, $\lambda = 0.2$, $\kappa = 0.05$, $N = 3.0$, OCR = 1. Pile–soil friction coefficient: 0)

All the solutions were obtained with the automatic scheme described previously using 1,000 coarse load steps. The ALE analyses for the fine mesh require approximately 6–8 h CPU time on an IBM T41 laptop with a 1.6 GHz Pentium processor and 1.5 GB RAM. The UL analyses for a coarse mesh, with one quarter of the elements in the fine mesh, require approximately 2–3 h of CPU time on the same machine. Allowing for the difference in the degrees of freedom in these meshes, we see the ALE method is almost as efficient as the UL method. A standard Newton–Raphson scheme (see [24]) was also tried with 10,000 load steps, but failed to provide a reasonable solution. The failures of the Newton–Raphson scheme were caused either by lack of convergence, or by numerical breakdown if the non-converged steps were allowed to continue.

Figure 11 shows the ALE mesh for a pile penetrating into a Modified Cam Clay (MCC) soil. The soil is fully drained and its properties are given in the figure: λ is the slope of the normal compression line (NCL), κ the slope of the unloading-reloading line, e_N the void ratio on the NCL when the mean stress is one unit (kPa), and OCR the overconsolidation ratio. The description and implementation of the specific MCC constitutive model in the finite element procedure can be found in Sheng et al. [22]. Because the MCC soil has a zero elastic bulk modulus at zero mean stress, the top layer of soil elements (0.05 m thick) was modelled using the Mohr–Coulomb model. The deformed meshes in Fig. 11 show that a part of the initial ground surface is in contact with the pile, and that the ALE meshes sustain the optimal form of the initial undeformed mesh. We can also notice that the ground
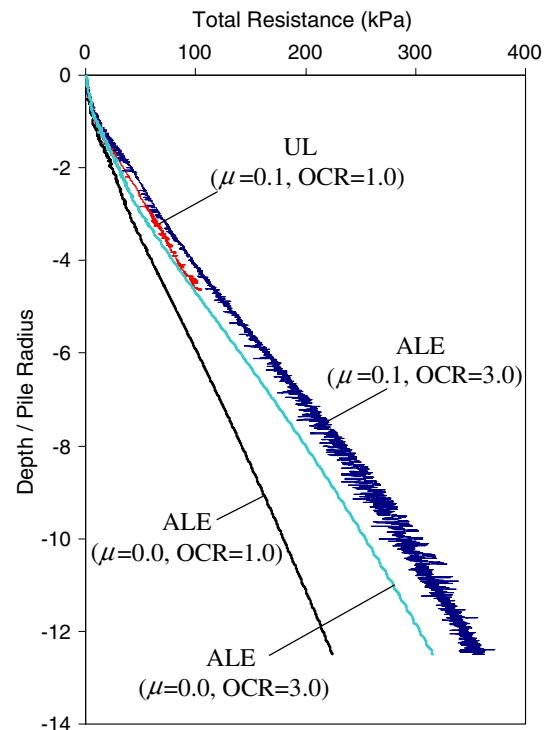
Fig. 12 Predicted load–displacement curves in Modified Cam Clay soil (μ: interfacial friction coefficient)

surface remains more or less at the same level as the pile penetrates, indicating that the total soil volume decreases. The load–displacement curves shown in Fig. 12 further demonstrate the effectiveness of the new algorithms in reducing

oscillations. It is noted that the UL analysis for a frictional pile does not finish with a complete solution, due to severe mesh distortion.

5 Conclusions

The ALE method presented in this paper is effective for handling the mesh distortion in penetration problems and does not cause much increase in the CPU time. The smooth discretisation of contact surfaces can reduce the oscillation in the load–displacement curves significantly, while the automatic load stepping scheme is more robust in solving the systems of nonlinear equations. These algorithms advance the simulation of penetration problems in geomechanics considerably. Additional enhancements may include the incorporation of mortar-based frictional contact formulation for higher order elements in the soil domain [4], the incorporation of element separation modelling and efficient contact search algorithms for group piles and 3D penetration problems, as well as the development of coupled displacement and pore pressure methods with dynamic effects.

References

1. Abbo AJ, Sloan SW (1996) An automatic load stepping algorithm with error control. Int J Numer Methods Eng 39:1737–1759
2. Benson DJ (1989) An efficient, accurate and simple ALE method for nonlinear finite element programs. Comp Methods Appl Mech Eng 72:305–350
3. Belytschko T, Kennedy JM (1978) Computer models for subassembly simulation. Nucl Eng Des 49:17–38
4. Fischer KA, Wriggers P (2006) Motar based frictional contact formulation for higher order interpolation using the moving friction cone. Comp Methods Appl Mech Eng 195(37–40):5020–5036
5. Fischer KA, Sheng D, Abbo AJ (2007) Modeling of pile installation using contact mechanics and quadratic elements. Comp Geotech 34(6):449–461
6. Gadala MS, Wang J (1998) ALE formulation and its application in solid mechanics. Comp Methods Appl Mech Eng 167:33–55
7. Ghosh S, Kikuchi N (1991) An arbitrary Lagrangian–Eulerian finite element method for large deformation analysis of elastic-viscoplastic solids. Comp Methods Appl Mech Eng 86:127–188
8. Hu Y, Randolph MF (1998) A practical numerical approach for large deformation problems in soils. Int J Numer Anal Methods Geomech 22:327–350
9. Huang W, Sheng D, Sloan SW, Yu HS (2004) Finite element analysis of cone penetration in cohesionless soil. Comp Geotech 31:517–528
10. Hughes TJR, Liu WK, Zimmermann TK (1981) Lagrangian–Eulerian finite element formulation for incompressible viscous flow. Comp Methods Appl Mech Eng 58:19–36
11. Laursen TA (2002) Computational contact and impact mechanics. Springer, Berlin
12. Liu WK, Belytschko T, Chang H (1986) An arbitrary Lagrangian–Eulerian finite element method for path-dependant materials. Comp Methods Appl Mech Eng 58:227–245
13. Liyanapathirana DS, Deeks AJ, Randolph MF (2000) Numerical modelling of large deformations associated with driving of open-ended piles. Int J Numer Anal Meth Geomech 24:1079–1101
14. Lopez RJ (2001) Advanced engineering mathematics. Addison Wesley, New York
15. Nazem M (2006) Numerical algorithms for large deformation problems in geomechanics. Ph.D. thesis, School of Engineering, The University of Newcastle, Australia
16. Nazem M, Sheng D, Carter JP (2006) Stress integration and meshing refinement for large deformation in geomechanics. Int J Numer Methods Eng 65:1002–1027
17. Peric D, Hochard C, Dutko M, Owen DRJ (1996) Transfer operators for solving meshes in small strain elasto-plasticity. Comp Methods Appl Mech Eng 137:331–344
18. Peric D, Vaz MJr, Owen DRJ (1999) On adaptive strategies for large deformations of elasto-plastic solids at finite strains: computational issues and industrial applications. Comp Methods Appl Mech Eng 176:279–312
19. Potts DM, Zdravkovic L (2001) Finite element analysis in geotechnical engineering, vol 1, theory. Thomas Telford, London
20. Sheng D, Axelsson K, Magnusson O (1997) Stress and strain fields around a penetrating cone. In: Pietruszczak S, Pande GN (eds) Numerical models in geomechanics. Balkema, Rotterdam, pp 653–660
21. Sheng D, Eigenbrod KD, Wriggers P (2005) Finite element analysis of pile installation using large-slip frictional contact. Comp Geotech 32(1):17–26
22. Sheng D, Sloan SW, Yu HS (2000) Aspects of finite element implementation of critical state models. Comput Mech 26:185–196
23. Sheng D, Sloan SW (2001) Load stepping methods for critical state models. Int J Numer Methods Eng 50:67–93
24. Sheng D, Wriggers P, Sloan SW (2006) Improved numerical algorithms for friction contact in pile penetration analysis. Comp Geotech 33:341–354
25. Sheng D (2007) Frictional contact for pile installation. In: Wriggers P, Nackenhorst U (eds) IUTAM symposium on computational methods in contact mechanics. Springer, Heidelberg, pp 239–256
26. Simo JC, Meschke G (1993) A new class of algorithms for classical plasticity extended to finite strains. Appl Geomater Computat Mech 11:253–278
27. Sloan SW, Randolph MF (1984) Numerical prediction of collapse loads using finite element methods. Int J Numer Anal Methods Geomechan 6:47–76
28. Susila E, Hryciw RD (2003) Large displacement FEM modelling of the cone penetration test (CPT) in normally consolidated sand. Int J Numer Anal Methods Geomech 27:585–602
29. Van den Berg P (1994) Analysis of soil penetration. Ph.D. thesis, Technische Universiteit Delft
30. Wang CX, Carter JP (2002) Deep penetration of strip and circular footings into layered clays. Int J Geomech 2(2):205–232
31. Wriggers P (2002) Computational contact mechanics. Wiley, Chichester
32. Yamada T, Kikuchi F (1993) An arbitrary Lagrangian–Eulerian finite element method for incompressible hyperelasticity. Comp Methods Appl Mech Eng 102:149–177
33. Yu HS (2004) Cavity expansion methods in geomechanics. Kluwer, Dordrecht
34. Zhou H, Randolph MF (2007) Computational techniques and shear band development for cylindrical and spherical penetrometers in strain-softening clay. Int J Geomech ASCE 7(4):287–295